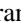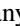# Periodic quantum Rabi model with cold atoms at deep strong coupling

Geram Hunanyan [1,*] Johannes Koch,[1] Stefanie Moll,[1] Enrique Rico [2,3,4,5] Enrique Solano,[6] and Martin Weitz [1]

[1]*Institut für Angewandte Physik, Universität Bonn, Wegelerstrasse 8, 53115 Bonn, Germany*
[2]*Department of Physical Chemistry, University of the Basque Country UPV/EHU, Box 644, 48080 Bilbao, Spain*
[3]*Donostia International Physics Center, 20018 Donostia-San Sebastián, Spain*
[4]*EHU Quantum Center, University of the Basque Country UPV/EHU, P.O. Box 644, 48080 Bilbao, Spain*
[5]*IKERBASQUE, Basque Foundation for Science, Plaza Euskadi 5, 48009 Bilbao, Spain*
[6]*Kipu Quantum, Greifswalder Straße 226, 10405 Berlin, Germany*

The quantum Rabi model describes the coupling of a two-state system to a bosonic field mode. Recent theoretical work has pointed out that a generalized periodic version of this model, which maps onto Hamiltonians applicable in superconducting qubit settings, can be quantum simulated with cold trapped atoms. Here, we experimentally demonstrate atomic dynamics predicted by the periodic quantum Rabi model far in the deep strong-coupling regime. The two-state system is represented by two Bloch bands of cold atoms in an optical lattice, and the bosonic mode by oscillations in a superimposed optical dipole trap potential. The observed dynamics beyond the usual quantum Rabi physics becomes relevant when the edge of the Brillouin zone is reached, and evidence for collapse and revival of the initial state is revealed at extreme coupling conditions.

## I. INTRODUCTION

The interaction of a two-state system with an oscillatory mode, as in a fully quantized form described by the quantum Rabi model, is among the most fundamental problems of quantum optics [1,2]. Experimental work on the interaction of two-level systems with quantized field modes has been carried out with Rydberg atoms in microwave cavities before being carried over to the optical domain [3]. The obtained experimental results, for which the coupling strength between the atoms and the electromagnetic field was above the decoherence rate, corresponding to the so-called strong-coupling regime, are described by the celebrated Jaynes-Cummings model, which predicts the emergence of hybrid matter-light eigenstates [4–11]. Other than the Jaynes-Cummings model, the quantum Rabi model (QRM) is valid for arbitrary coupling strengths, given that beyond the co-rotating terms, it also accounts for the counter-rotating terms of the interaction Hamiltonian, which leads to counterintuitive effects as that excitations can be created out of the vacuum. The quantum Rabi physics becomes relevant as the coupling strength $g$ becomes comparable or even exceeds the bosonic mode frequency $\omega$, with the regime $g/\omega \geqslant 1$ being termed the deep strong-coupling (DSC) regime. Experimentally, quantum Rabi physics has been studied with

superconducting Josephson systems, metamaterials, ion trapping, and with cold atom settings [12–16]. In recent work, by encoding the two-level system in the occupation of Bloch bands of cold trapped atoms, we have demonstrated quantum Rabi dynamics far in the DSC regime at interaction times at which the dynamics remains within the first Brillouin zone [17].

Here, we report the observation of collapse and revival of quantum Rabi dynamics in the DSC regime with cold trapped atoms. We monitor the atomic evolution at long interaction times beyond the first Brillouin zone, with the two-level system being encoded in the Bloch band structure and the bosonic mode in the oscillatory motion of a superimposed optical dipole trapping potential. In the investigated regime, the fact that the qubit information is stored in the band structure becomes significant such that the predictions of the QRM and the periodic quantum Rabi model (pQRM) differ because half of the phase space available to the QRM is mapped to the external atomic structure. The pQRM can be considered as a generalization of the QRM, where the growth of the bosonic excitations is truncated at an earlier stage, generating an echolike periodic cycle with doubled temporal periodicity. It essentially acts as a different light-matter interaction, emerging in a unique manner from the experimental context of cold atoms in variable potentials. The achieved normalized coupling strength of $g/\omega \simeq 6.5$, meaning that the coupling clearly dominates over all other relevant system energies, compares favorably to the parameters of state-of-the-art works of $g/\omega \simeq 1.9$ obtained in the phase space of superconducting fluxonium systems [18]. In our work, both collapse and revival of the excitation number are observed, as well as phase dependence of the prepared Schrödinger catlike states. We attribute our experimental data to give evidence for a quantum

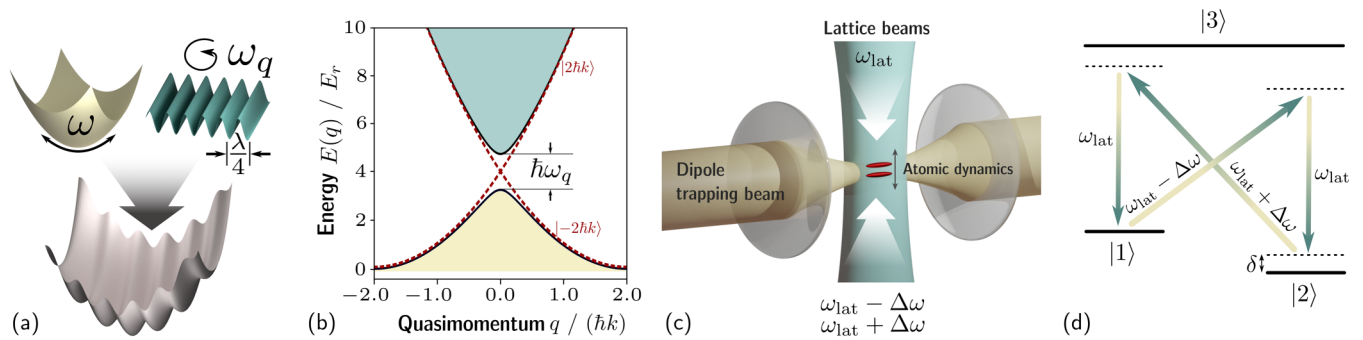*Contact author: hunanyan@iap.uni-bonn.de

FIG. 1. (a) Cold rubidium atoms are subjected to the potential obtained by superimposing a harmonic trap (left) and a periodic lattice potential (right). The image also shows the corresponding oscillatory modes: an oscillation mode at frequency $\omega$ in the harmonic potential and a mode at frequency $\omega_q$ at the first band gap of the lattice. In the combined potential, the coupling of modes can exceed their eigenfrequencies. (b) Atomic dispersion relation in a lattice of spatial periodicity $\lambda/4$. (c) Scheme of the setup. A near-the-center harmonic confinement for cold rubidium atoms is realized with a focused dipole trapping laser beam. The additional high spatial periodicity lattice potential is realized by driving with an optical beam of frequency $\omega_{\text{lat}}$ and two counterpropagating components with frequencies $\omega_{\text{lat}} + \Delta\omega$ and $\omega_{\text{lat}} - \Delta\omega$; see (d) for the coupling scheme.

simulation of the periodic quantum Rabi model (pQRM) in an atomic, molecular, and optical (AMO) physics system at deep strong coupling.

## II. THEORETICAL DESCRIPTION

The basic principle of the scheme realized in our work is shown in Fig. 1. Figure 1(a) illustrates the two quantum mechanical oscillation modes relevant here, which in the first case are generated by the oscillation of atoms in a harmonic trap potential, and in the second case by Bragg reflection in a lattice potential from the splitting of the two lowest Bloch bands, the latter realizing a two-state system. The superposition of the two potentials leads to an extremely strong coupling of the two quantized atomic oscillation modes. In our implementation, the harmonic trap potential is generated by a focused optical dipole trapping beam and the superimposed lattice potential via the dispersion of multiphoton Raman transition [19,20], resulting in a spatial periodicity of $\lambda/4$, where $\lambda$ is the wavelength of the driving optical beams. Formally, the system can be described by the Hamiltonian

$$\hat{\mathcal{H}} = \frac{\hat{p}^2}{2m} + \frac{m\omega^2}{2}\hat{x}^2 + \frac{V}{2}\cos(4k\hat{x}), \qquad (1)$$

where $\hat{x}$ and $\hat{p}$ are the position and momentum operators, $m$ is the atomic mass, $V$ is the lattice depth, $k = 2\pi/\lambda$, and $\omega$ is the harmonic trap frequency. Figure 1(b) shows the dispersion relation of atoms in the lattice in a representation that is centered around the position of the first band crossing at $p = \pm 2\hbar k$ as a function of the atomic quasimomentum $q$. At the band crossing, i.e., at $q = 0$, the eigenstates of the two-level system are given by $|g\rangle = \frac{1}{\sqrt{2}}(|-2\hbar k\rangle + |+2\hbar k\rangle)$ and $|e\rangle = \frac{1}{\sqrt{2}}(|-2\hbar k\rangle - |+2\hbar k\rangle)$, respectively.

We introduce an eigenbasis of the momentum operator $|k\rangle = |q, n_b\rangle$ such that the description of the momentum eigenvalue is split into a continuous part $q$ defined in the interval $(-2\hbar k, 2\hbar k]$ and an integer part $n_b \in \mathcal{Z}$ that defines a band index. The wave functions for these states are given by $\langle x|q, n_b\rangle = e^{iqx/\hbar}e^{-i2kx}e^{i4n_bkx}$. The position operator $\hat{x}$ can

be represented by the derivative of the quasimomentum $q$ within a band, i.e., $\hat{x} = -i\hbar\frac{\partial}{\partial q}$, but will also induce a coupling between the bands at the boundaries of the interval (see Appendix B). Within a band, the Hamiltonian of the system is just given by the harmonic term, $\hat{q}^2/2m + (m/2)\omega^2\hat{x}^2 = \hbar\omega(\hat{a}^\dagger\hat{a} + 1/2)$, where $\hat{a}^\dagger = \sqrt{\frac{m\omega}{2\hbar}}(\hat{x} - \frac{i}{m\omega}\hat{q})$ is the creation operator of the bosonic field mode. If we project onto the two lowest bands $n_b = \{0, 1\}$, the structure of a two-level system (qubit) appears. Within the first Brillouin zone, the resulting quantum Rabi Hamiltonian can be written as

$$\hat{\mathcal{H}}_{\text{QRM}} = \hbar\omega\hat{a}^\dagger\hat{a} + \frac{\hbar\omega_q}{2}\hat{\sigma}_z + i\hbar g\hat{\sigma}_x(\hat{a}^\dagger - \hat{a}). \qquad (2)$$

Here, $\hat{\sigma}_x$ and $\hat{\sigma}_z$ are Pauli matrices acting on coarse-grained wave functions in upper and lower bands, respectively, while $\hbar\omega_q$ denotes the splitting between bands corresponding to the qubit spacing and with a coupling $g = k\sqrt{2\hbar\omega/m}$. Formally, the quantum Rabi Hamiltonian of Eq. (2) is derived from Eq. (1) in the absence of an Umklapp term [21]. The complete dynamics also has a boundary term (see Appendix B), which introduces the notion of a periodic quantum Rabi model (pQRM) and is the subject of this manuscript. As we will see below, already at an early stage of the evolution, exactly at $\omega t/2\pi = 0.25$, the wave function of the collective system experiences an echolike return such that the collapse and revival dynamics is modified. Interestingly, characteristic signatures of the pQRM, such as a modified pattern of collapse and revival compared to the QRM, can be described analytically by using a perturbative approach in a position-momentum $(x, p)$ phase space picture, as shown in Appendix D.

Given that the two-level system in the used quantum Rabi implementation is stored in the band structure, effects beyond the usual quantum Rabi physics can arise when one reaches the edge of the first Brillouin zone. For the lattice that is used here, with spatial periodicity $\lambda/4$, the relation between momentum and quasimomentum for the first two bands [see, also, Fig. 1(b)] is $q = p - 2\hbar k$ for $p \geqslant 0$ and $q = p + 2\hbar k$ for $p < 0$, respectively, such that the quasimomentum is restricted to $q \in (-2\hbar k, 2\hbar k]$. Essentially, storage of the qubit in the band structure itself introduces a folding in the Bloch band

structure. This results in collapse and revival effects that are distinctly modified with respect to predictions of the original QRM.

## III. EXPERIMENTAL SETUP AND PROCEDURE

Our setup [see also, the schematics of Fig. 1(c)] is a modified version of an apparatus used in earlier works [17,19,20]. Initially, a Bose-Einstein condensate of rubidium atoms ($^{87}$Rb) in the $m_F = -1$ spin projection of the $F = 1$ ground state is produced in the quasistatic optical dipole trapping potential imprinted by a focused beam emitted by a $CO_2$ laser operating near 10.6 µm wavelength. The beam power $P$ is then adiabatically increased to reach a desired value of the trapping frequency $\omega \propto \sqrt{P}$ for quantum Rabi manipulation. Atoms are, in addition, exposed to a high spatial ($\lambda/4$) periodicity lattice potential, where $\lambda = 783.5$ nm denotes the wavelength of the driving laser beams. The potential of the corresponding periodicity is generated by off-resonantly driving four-photon Raman transitions between the $m_F = -1$ and $m_F = 0$ ground-state sublevels of $F = 1$ over the $5P_{3/2}$ excited-state manifold using a beam of frequency $\omega_{lat}$ and two superimposed counter-propagating beams of frequencies $\omega_{lat} + \Delta\omega$ and $\omega_{lat} - \Delta\omega$ [Fig. 1(d)]. Following the adiabatic intensity ramp of the dipole trapping beam, atoms are prepared at the position of the first band crossing of the high spatial periodicity lattice [see, also, the dispersion relation of Fig. 1(b)] by means of Bragg diffraction. After subsequent activation of the lattice beams, atoms are exposed to the combined potential as indicated in Fig. 1(a). Typical experimental parameters are harmonic trapping frequencies $\omega/2\pi \in [350, 750]$ Hz, resulting in normalized coupling $g/\omega \in [4.1, 6.5]$, which is far in the DSC regime. The investigated regime for the two-level qubit splitting is $\omega_q/2\pi \in [0, 5.5]$ kHz.

At the end of the atom manipulation phase, both the lattice beams and the dipole trapping beam are extinguished, after which absorption imaging is employed for detection. In the course of the measurements, data were recorded analyzing the real-space distribution, as probed by imaging directly after manipulation, as well as recording of the momentum distributions, for which time-of-flight imaging was used. For the former measurements, except when recording mean displacements, data analysis was performed after deconvolution with the determined point spread function of the imaging system, as to reduce systematic effects stemming from the $\simeq 6.5$ µm instrumental resolution of our imaging system. For the present measurements investigating long interaction times of quantum Rabi manipulation, relatively low atom numbers ($\sim$800) are used, to reduce interaction effects.

## IV. RESULTS AND DISCUSSION

To begin with, we have investigated the temporal evolution of the bosonic excitation number $\langle N \rangle$, with $\hbar\omega(\langle N \rangle + \frac{1}{2}) = \frac{m\omega^2}{2}\langle x^2 \rangle + \frac{1}{2m}\langle q^2 \rangle$, for times up to and beyond the expected revival. Atoms were initially prepared at the trap center with a momentum of $p = -2\hbar k$, for which the quasimomentum $q$ vanishes. The data points in Fig. 2(a) give the temporal variation of the mean excitation number, as derived from the rms spread of the experimental *in situ* and time-of-flight
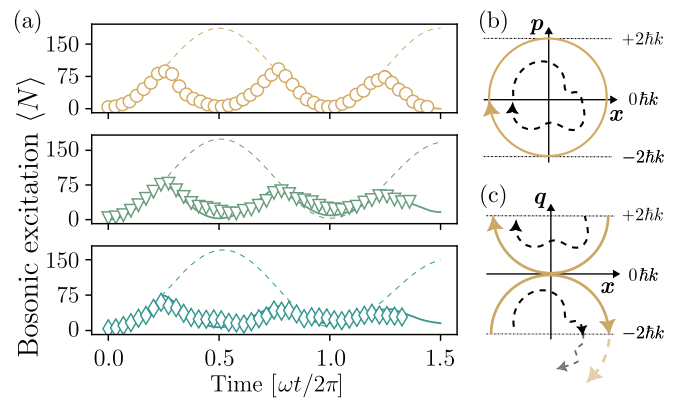


FIG. 2. (a) Temporal evolution of the number of excitations, $\langle N \rangle$, for a qubit splitting $\omega_q/2\pi \to 0$ (top), 800(14) Hz (middle), and 1280(21) Hz (bottom), and a harmonic trapping frequency of $\omega/2\pi = 346(8)$ Hz (relative coupling $g/\omega \simeq 6.53$). Atoms were initially prepared at a momentum of $p = -2\hbar k$. The solid lines are theory predictions based on the pQRM, and the dashed line for the (usual) QRM. (b) Illustration of the temporal evolution of atomic wave packets in phase space ($x$: position; $p$: momentum) for $\omega_q = 0$ (yellow solid line) and $\omega_q > 0$ (black dashed line), respectively. (c) As in (b), now plotted in a position ($x$)–quasimomentum ($q$) representation. The transparent dashed lines indicate the corresponding trajectories predicted in the (usual) QRM, for which no remapping of $q$ onto the Brillouin zone of the lattice occurs.

imaging data, versus the interaction time of quantum Rabi manipulation, for different lattice depths $V = 2\hbar\omega_q$ [top to bottom: $\omega_q/2\pi \to 0$, 800(14) Hz, and 1280(21) Hz]. We observe a periodic pattern of the excitation number oscillating with a half temporal period of the harmonic potential $T = 2\pi/\omega$, which, for larger qubit spacings, reduces in magnitude, creating the pQRM. The experimental data are in good agreement with theoretical pQRM predictions; see Eq. (1) with the described identifications between $p$ and $q$ as to keep the quasimomentum $q$ in the first Brillouin zone. However, the observed physics does not follow the QRM predictions of Eq. (2); see the solid and dashed lines, respectively. Figures 2(b) and 2(c) qualitatively illustrate the expected atomic dynamics in position ($x$)–momentum ($p$) and position ($x$)–quasimomentum ($q$) phase-space representations, respectively (see also, Appendix A for corresponding experimental measurements). Here, the yellow solid line gives the expected variation for the trivial case of $\omega_q = 0$, which corresponds to a usual (shifted) harmonic oscillator dynamics in position-momentum (position-quasimomentum) space, respectively, and the dashed line illustrates an example for the nontrivial case of $\omega_q > 0$. The observed temporal variations of the mean excitation number [Fig. 2(a)], given it is proportional to the rms distance from the origin in position-quasimomentum space, of half the harmonic oscillator period $T = 2\pi/\omega$, is well understood from the corresponding trajectories, at least for not-too-large values of $\omega_q$. For comparison, the dashed lines in Fig. 2(c) illustrate the expected behavior predicted in the (original) quantum Rabi model [Eq. (2)], for which the periodicity equals the full harmonic oscillator cycle. To study the effects of the band mapping in more detail, we have analyzed the temporal variation of the mean Bloch
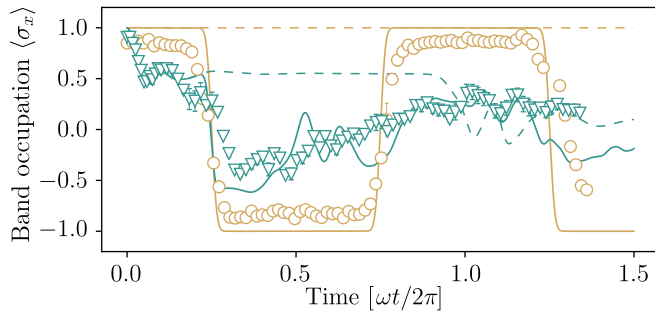
FIG. 3. Temporal variation of the average value of the Bloch band occupation $\langle \sigma_x \rangle$ for $\omega/2\pi = 346(8)$ Hz and qubit spacings of $\omega_q/2\pi \rightarrow 0$ (yellow circles) and 1750(25) Hz (green triangles). The solid and dashed lines are theory predictions for the pQRM and the usual QRM, respectively.
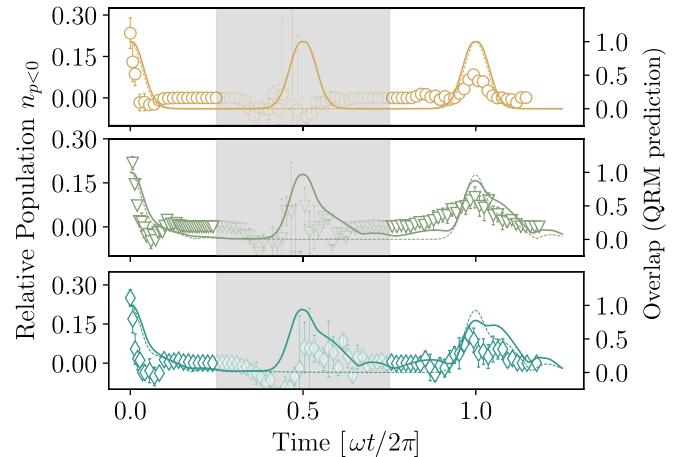


FIG. 4. Collapse and revival of an initial state. The data points give the relative number of atoms, $n_{p<0} = (N_{p<0} - -N_{p>0})/(N_{p<0} + N_{p>0})$, with $N_{p<0}$ ($N_{p>0}$) as the atom number detected with momentum $p < 0$ ($p > 0$), vs the interaction time for $\omega/2\pi = 650(21)$ Hz and qubit splittings $\omega_q/2\pi \rightarrow 0$ (top), 800(14) Hz (middle), and 1280(21) Hz (bottom). The solid lines are theory for the pQRM, and the dashed lines give the overlap with the initial state (see scale on the right-hand side) as predicted in the (usual) QRM. The gray shaded area indicates regions where the experimental signal is affected by large instrumental phase fluctuations.

band occupation $\langle \sigma_x \rangle$, which can be expressed in the basis of the band eigenstate numbers $\hat{\sigma}_x = |n_b = 0\rangle \langle n_b = 0| - |n_b = 1\rangle \langle n_b = 1|$, with $n_b = 0, 1$ for $p = q - 2\hbar k$ and $p = q + 2\hbar k$, respectively. The corresponding experimental data are shown in Fig. 3 for different qubit splittings. While at small lattice depth the expectation value of the band index remains constant until the edge of the Brillouin zone is reached and the bands are remapped, at higher lattice depth the modulus of $\langle \sigma_x \rangle$ reduces and oscillations are observed (visible most clearly near times $t = 0$ and $2\pi/\omega$), as attributed to the Rabi oscillations between the momentum states $\pm 2\hbar k$, respectively. The oscillations are suppressed at smaller values of $\omega_q$ since then the coupling term, which is proportional to $\hat{\sigma}_x$ [22], dominates over all other energy scales and appear only for larger values of the qubit splitting, upon which the dispersive DSC regime is reached. Corresponding behavior for small interaction times has also been observed in an earlier work of our groups [17], and the present results generalize these observations to beyond the first Brillouin zone. In subsequent measurements, we have prepared atomic wave packets in the qubit eigenstates of the system, which are superpositions of momentum picture eigenstates. For this, atoms were irradiated by two simultaneously performed Bragg pulses of counterpropagating momentum transfer, such that depending on the relative phase, different qubit initial states can be prepared. Figure 4 gives data investigating the collapse and revival of an initially prepared qubit eigenstate $|g\rangle = \frac{1}{\sqrt{2}}(|-2\hbar k\rangle + |+2\hbar k\rangle)$ for a harmonic trap frequency $\omega/2\pi \simeq 650$ Hz ($g/\omega \simeq 4.8$) and different values of the lattice depth. For the measurement, after a variable interaction time in the combined potential, a $\pi/2$ four-photon Raman pulse tuned to drive transfer between the momentum states $-2\hbar k$ and $2\hbar k$ was applied such that when the initial state is fully revived, atoms are transferred to the momentum state $-2\hbar k$ and we have $\sigma_z = 1$. The vertical scale of the plots in Fig. 4 shows the relative number of atoms observed with a negative momentum ($p < 0$) in the time-of-flight images with respect to the total atom number, which constitutes a measurement of $\langle \sigma_z \rangle$. The top plot corresponds to a vanishing lattice depth ($\omega_q \rightarrow 0$) such that this experiment realizes a trapped atom interferometer, and shows a revival at a full oscillation time of $t = 2\pi/\omega$. The middle and lower panels, as recorded for increased lattice depth, show revivals with visible substructures. The

experimental data qualitatively agree with predictions based on the periodic quantum Rabi model (solid lines), and we attribute the reduced contrast of the revival signal mainly to the finite atomic velocity distribution. The shaded area at near half the revival time corresponds to a region where large phase fluctuations, attributed to mechanical vibrations of the Raman beams with respect to the dipole trapping beam, become relevant due to the reversed propagation direction of the atomic wave-packet paths with respect to preparation given here, and we consider this region as inaccessible to the experiment. For comparison, the dashed line gives the expected overlap of the initial state predicted in the (standard) quantum Rabi model, for which no revival at half the oscillation time is expected.

To study the dependence of pQRM evolution on the qubit state encoded in the Bloch band structure, we have analyzed the number of created system excitations when initially preparing atoms in both eigenstates $|g\rangle = \frac{1}{\sqrt{2}}(|-2\hbar k\rangle + |+2\hbar k\rangle)$ and $|e\rangle = \frac{1}{\sqrt{2}}(|-2\hbar k\rangle - |+2\hbar k\rangle)$. Figure 5(a) gives experimental data for the difference in the correspondingly obtained excitations versus time for different lattice depths. We observe a clear difference in the number of created excitations for two different relative phases used at qubit splitting above near $\omega_q/2\pi \simeq 700$ Hz. This is in agreement with theory [Fig. 5(b)], though in the experiment again the contrast is reduced. As an example, Fig. 5(c) gives a plot of the temporal variation of the difference in observed excitations for $\omega_q/2\pi \simeq 1250$ Hz. Formally, at a small qubit splitting, the oscillating wave packets can be well described as Schrödinger cat states, while they become highly entangled states at larger values of the qubit splitting. The agreement of the experimental data with the theory is evidence that coherence is maintained in the dispersive DSC regime of the pQRM.
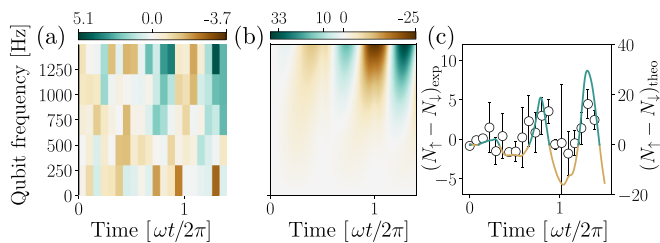
FIG. 5. (a) Difference $(N_\uparrow - N_\downarrow)$ of observed mean excitation numbers between when initially preparing atoms in the upper and lower qubit states $N_\uparrow$ and $N_\downarrow$ vs both the interaction time and the qubit spacing $\omega_q/2\pi$, in a color-coded representation for $\omega/2\pi \simeq 350$ Hz, $g/\omega \simeq 6.53$. (b) Corresponding theory. (c) Data for $\omega_q/2\pi = 1250(23)$ Hz exemplary drawn as a diagram, along with theory (solid line).

## V. CONCLUSIONS

To conclude, we have observed collapse and revival effects of the dynamics in a cold atom based quantum simulation of the quantum Rabi physics at extreme parameter regimes. Our experimental data are in good agreement with theory based on a generalized, periodic variant of the usual QRM, the physical origin being the periodic nature of the atomic Brillouin zone of cold atoms in a lattice.

In the future, it would be interesting to generalize the reported observations to using atoms with tunable interactions using Feshbach tuning (e.g., $^{85}$Rb or $^{39}$K), such that both the limits of negligible and stronger interactions can be explored. Other perspectives, inspired also by the formal analogy of the system Hamiltonian to superconducting qubit systems, include quantum information processing applications [23–25], as well as the search for novel quantum phase transitions [26,27].

## APPENDIX A: ADDITIONAL DATA AND EXPERIMENTAL DETAILS

The near harmonic trapping potential for the cold cloud of rubidium atoms is generated with a focused laser beam (46 $\mu$m diameter) derived from a $CO_2$ laser operating at near 10.6 $\mu$m wavelength. Despite the large detuning of the midinfrared radiation from the lowest electronic resonances (the rubidium D-lines) which results in a very low heating rate from

spontaneous scattering, the quasistatic atomic polarizability leads to a confining potential. Both the optical lattice and the optical Bragg pulses are generated using optical radiation derived from a high-power diode laser operating near $\lambda \simeq 783.5$ nm wavelength, which is detuned by approximately 3.3 nm to the red of the rubidium D2-line. The laser emission is split into two, and each of the partial beams pass an acousto-optic modulator (AOM) used to imprint different optical frequency components and then coupled into optical fibers and guided to the vacuum chamber in which the cold atom experiment takes place. The optical lattice potential, which has a spatial periodicity of $\lambda/4$, is generated by the dispersion of Doppler-sensitive Raman transitions [19]. For this [see, also, Figs. 1(c) and 1(d) of the main text], atoms are irradiated with two copropagating beams of frequencies $\omega_{\text{lat}} + \Delta\omega$ and $\omega_{\text{lat}} + \Delta\omega$ and one counterpropagating beam of frequency $\omega$. Here, the $m_F = -1$ and the $m_F = 0$ spin projections of $F = 1$ are the ground states of the three-level scheme that is used, while the $5^2P_{3/2}$ manifold serves as the electronically excited state. We use a frequency offset between counterpropagating beams of $\Delta\omega/2\pi \simeq 945$ kHz, which is large enough to suppress unwanted standing-wave two-photon processes. A magnetic bias field of $B = 1.7$ G removes the degeneracy of the Zeeman sublevels, and the used value of the two-photon detuning [see, also, Fig. 1(d)] is $\delta/2\pi \simeq 210$ kHz. The optical fields exchange momentum with the atoms in units of four photon recoils, which is a factor of two above the corresponding process in a usual standing-wave lattice, resulting in a $\lambda/4$ spatial periodicity of the generated lattice potential. We next give additional experimental data regarding the measurement shown in Fig. 3, showing the temporal evolution of the Bloch band occupation in the combined lattice and harmonic trap for quantum Rabi manipulation. Figure 6 gives the observed corresponding temporal evolution of mean values of the atomic position $\langle x \rangle$ and quasimomentum $\langle q \rangle$. As described in the main text, atoms here were initially prepared at a momentum of $p = -2\hbar k$ and, in the trap center, the used bosonic mode frequency is $\omega/2\pi = 346(8)$ Hz, and the qubit spacing is $\omega_q/2\pi \to 0$ (yellow circles) and 1750(25) Hz (green triangles). In all cases, the experimental data compare well with predictions based on the periodic quantum Rabi model. Note that the experimental resolution of the imaging system (6.5 $\mu$m) is comparable to the trapped atomic cloud size, which limits the significance of a detailed analysis of the real-space data. Nevertheless, the measurements allow us to qualitatively validate the illustrations for the expected atomic wave-packet trajectories indicated in Figs. 2(b) and 2(c).

Figure 7 gives examples of the obtained time-of-flight imaging data, as employed to evaluate the atomic momentum distribution at the end of quantum Rabi manipulation in the combined lattice and harmonic trap potential. The used free expansion time is 8 ms, after which an absorption image was recorded on a sCMOS camera. To begin with, Fig. 7(a) shows an absorption image recorded to analyze the atomic velocity distribution directly after preparing atoms in the qubit state, $|g\rangle = \frac{1}{\sqrt{2}}(|-2\hbar k\rangle + |2\hbar k\rangle)$, corresponding to a superposition of two counterpropagating momentum picture states, and Fig. 7(b) shows an image after applying a $\pi/2$-four-photon Raman pulse in addition, resulting in transfer of atoms predominantly to state $|-2\hbar k\rangle$. As described
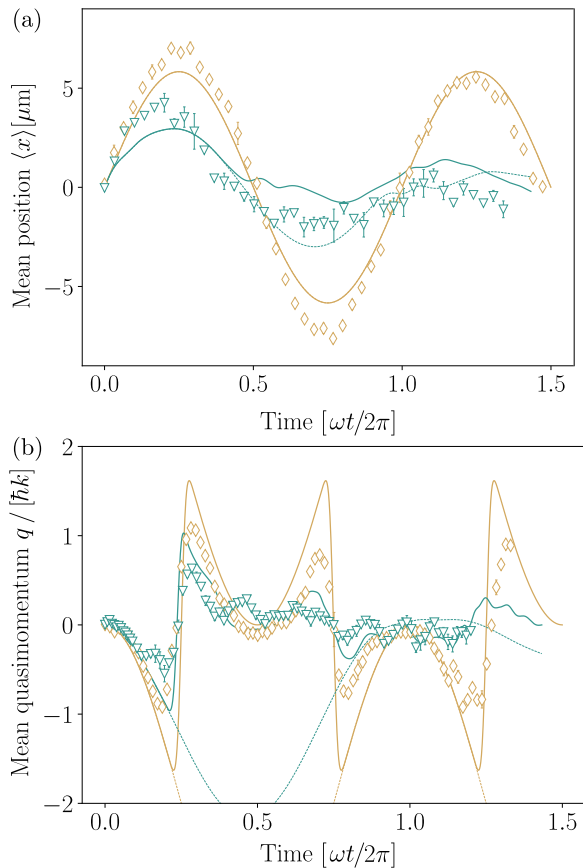
FIG. 6. Temporal evolution of the measured values for (a) the mean atomic position $\langle x \rangle$ and (b) the mean quasimomentum $\langle q \rangle$, for $\omega_q/2\pi \to 0$ (yellow data points) and $\omega_q/2\pi = 1750(25)$ Hz (green data points), along with theory based on the periodic quantum Rabi model (solid lines) and the (usual) quantum Rabi model (dashed lines). Experimental parameters are as in Fig. 3.

in the main text, from the data, visible finite transfer efficiency is attributed to the atomic velocity distribution. Next, Fig. 7(c) shows a series of time-of flight images recorded after different atomic interaction times in the harmonic trap potential, again with atoms initially prepared in the qubit state,

$|g\rangle = \frac{1}{\sqrt{2}}(|-2\hbar k\rangle + |2\hbar k\rangle)$, as a superposition of counterpropagating wave packets, and after the interaction time in the harmonic trap applying a $\pi/2$-four-photon Raman pulse, as to provide exemplary raw data for the top plot ($\omega_q/2\pi = 0$) of Fig. 4. Both at near half the oscillation time and at a full oscillation time ($T = 2\pi/\omega$), an enhanced population for atoms at negative final momentum $p < 0$ is observed, as understood from the rephasing of the wave packets. Given that this corresponds to a single realization of the experiment, phase fluctuations between the trapping and Raman beams do not affect the contrast, and the presence of revivals at both half and full oscillation times is well understood. Upon subsequent realizations of the experiment, only the data at a full revival remain phase stable.

## APPENDIX B: THEORETICAL METHODS

### 1. Periodic term of the Hamiltonian

The system is composed of a cloud of ultracold atoms exposed to two laser-induced potentials: a periodic lattice and a harmonic trap. When the atom density is sufficiently low, interactions among the atoms are negligible and the system can be described with a single-particle Hamiltonian,

$$\hat{H} = \frac{\hat{p}^2}{2m} + \frac{V}{2}\cos(4k\hat{x}) + \frac{m\omega^2}{2}\hat{x}, \qquad (B1)$$

where $\hat{p} = -i\hbar\frac{\partial}{\partial x}$ and $\hat{x}$ are the momentum and position of an atom of mass $m$, respectively. Here, $\omega$ is the angular frequency of the atom motion in the harmonic trap, while $V$ and $4k$ are the depth and wave vector of the periodic potential, respectively. The periodic lattice results from a four-photon interaction with a driving field of wave vector $k$.

We will assume that the harmonic trap is slowly varying on the length scale of the periodic potential. Under this assumption, the most suitable basis is given by the Bloch functions $\langle x|\phi_n(x)\rangle = e^{iqx/\hbar}e^{-i2kx}e^{i4nkx}$, where the first Brillouin zone is defined $q \in (-2\hbar k, 2\hbar k]$ and the band index $n \in \mathbb{Z}$.

It is straightforward to see that the momentum operator is diagonal in the Bloch basis, while the periodic potential introduces a coupling between adjacent
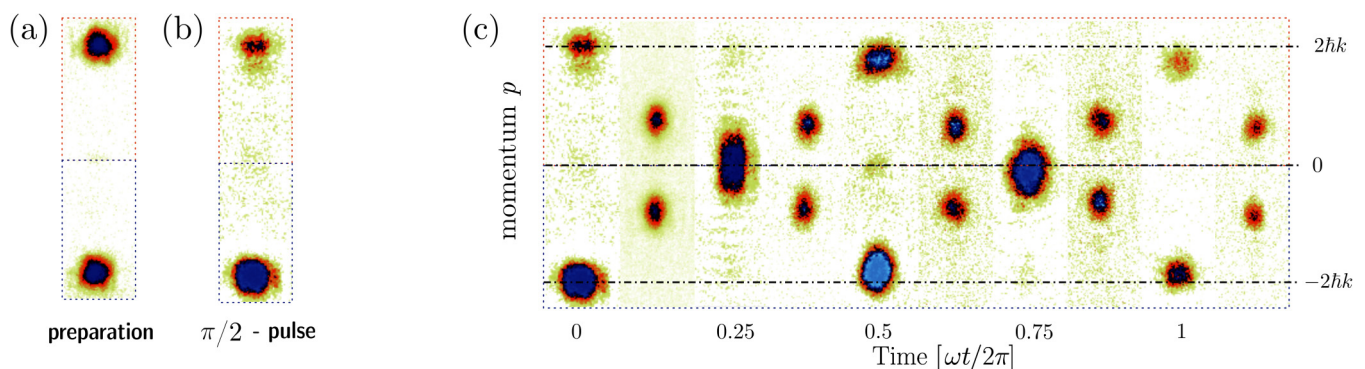


FIG. 7. (a) Time-of-flight image analyzing the atomic momentum distribution following the preparation of atoms in the qubit state, $|g\rangle = \frac{1}{\sqrt{2}}(|-2\hbar k\rangle + |2\hbar k\rangle)$. (b) Image recorded following an additional $\pi/2$ four-photon Raman pulse. (c) Series of time-of flight images recorded with an additional, variable delay between the preparation pulse and the final $\pi/2$ readout pulse.

bands,

$$\frac{\hat{p}^2}{2m} + \frac{V}{2}\cos(4k\hat{x})|q, n\rangle$$

$$= \frac{1}{2m}[q + (2n-1)2\hbar k]^2|q, n\rangle$$

$$+ \frac{V}{4}(|q, n+1\rangle + |q, n-1\rangle). \quad (B2)$$

Assuming that the system dynamics is restricted to the two bands with the lowest energy, the periodic part of the Hamiltonian can be rewritten in the Bloch basis as

$$\hat{H}_p = \frac{q^2}{2m} + \frac{2\hbar k}{m}\sigma_z q + \frac{V}{4}\sigma_x. \quad (B3)$$

Hence, the periodic potential allows one to encode the two-level system in the lowest two bands of the Bloch band structure. If the dynamics is kept in the same band, the harmonic potential introduces an operator which can be expressed as $\hat{x} = -i\hbar\frac{\partial}{\partial q}$ in the Bloch basis. This allows us to define the quasimomentum operator $\hat{q}$ and the position operator $\hat{x}$, which satisfy the usual commutation relation $[\hat{x}, \hat{p}] = i\hbar$.

In this way, we can rewrite the Hamiltonian as

$$\hat{H} = \frac{\hat{q}^2}{2m} + \frac{m\omega^2}{2}\hat{x}^2 + \frac{2\hbar k}{m}\sigma_z\hat{q} + \frac{V}{4}\sigma_x. \quad (B4)$$

### 2. Quadratic potential in the Bloch basis

Let us now discuss the quadratic term $\frac{m\omega^2}{2}\hat{x}^2$ in the main Hamiltonian. In the Bloch basis, we can write

$$\langle \tilde{q}, \tilde{n}|\hat{x}^2|q, n\rangle = \int_{-\infty}^{+\infty} dx\, x^2 e^{i[4(n-\tilde{n})k + (q-\tilde{q})/\hbar]x}. \quad (B5)$$

Considering diagonal elements in the qubit Hilbert space, i.e., setting $\tilde{n} = n$, we have

$$\langle \tilde{q}, n|\hat{x}^2|q, n\rangle = \int_{-\infty}^{+\infty} dx\, x^2 e^{i(q-\tilde{q})x/\hbar} = -\hbar^2\langle \tilde{q}, n|\frac{\partial^2}{\partial q^2}|q, n\rangle. \quad (B6)$$

Hence, we see that the harmonic potential introduces an operator, diagonal in the qubit Hilbert space, which can be expressed as $\hat{r} = -i\hbar\frac{\partial}{\partial q}$, in the Bloch basis. This allows us to define the quasimomentum operator $\hat{q}$ and the position operator $\hat{r}$, which satisfy the commutation relation $[\hat{r}, \hat{q}] = i\hbar$. On the other hand, for $\tilde{n} = n$, the integral is different from zero only if $4\hbar(n-\tilde{n})k = q - \tilde{q}$. Hence, the quadratic potential introduces a coupling between neighboring bands, for states whose momenta satisfy $4\hbar k = q - \tilde{q}$, of the kind $(|2\hbar k, n_b\rangle\langle-2\hbar k, n_b + 1| + \text{H.c.})$. This effective coupling is due to the periodicity of the quasimomentum, which mixes the bands $n = \{0, 1\}$ at the boundaries of the Brillouin zone. Such a coupling can be neglected as far as the system dynamics involves only values of the quasimomentum $\hat{q}$ included within the first Brillouin zone.

## APPENDIX C: MAPPING TO FLUXONIUM SYSTEMS

The fluxonium system is a circuit where we have, in parallel, a capacitor, an inductor, and a Josephson junction, when the energies of each of the elements are, in comparison with

one another, $E_J > E_C > E_L$. An analogy between the periodic quantum Rabi model presented in the main text and a superconducting fluxonium system [18] can be shown in the following. In principle, we only have one active node $a$. The equation of the flux going through this node is

$$C\ddot{\phi}_a = -\frac{\phi_a}{L} - J\sin\left(\frac{2\pi(\phi_a + \Phi_{\text{clas}})}{\Phi_0}\right), \quad (C1)$$

where $\Phi_{\text{clas}}$ is the external magnetic flux going through the spire defined by the Josephson junction and the inductor. From these equations, we can propose the following Lagrangian:

$$\mathcal{L}_{\text{Flux}} = \frac{C}{2}\dot{\Phi}_a^2 - \frac{\Phi_a^2}{2L} + \frac{J\Phi_0}{2\pi}\cos\left(\frac{2\pi(\phi_a + \Phi_{\text{clas}})}{\Phi_0}\right). \quad (C2)$$

With this, we are already in the situation of obtaining the Hamiltonian,

$$H = \frac{q_a^2}{2C} + \frac{\Phi_a^2}{2L} - \frac{J\Phi_0}{2\pi}\cos\left(\frac{2\pi(\phi_a + \Phi_{\text{clas}})}{\Phi_0}\right). \quad (C3)$$

We will rewrite it as follows:

$$H = 4E_C n_a^2 + \frac{1}{2}E_L\Phi_a^2 - E_J\cos\left(\frac{2\pi(\phi_a + \Phi_{\text{clas}})}{\Phi_0}\right), \quad (C4)$$

where we have defined $E_C = 2e/8C$, $n = q/2e$, $E_L = 1/L$, and $E_J = \frac{J\Phi_0}{2\pi}$. After this, we will have to quantize the system, therefore getting

$$\hat{H} = 4E_C\hat{n}_a^2 + \frac{1}{2}E_L\hat{\Phi}_a^2 - E_J\cos\left(\frac{2\pi(\hat{\phi}_a + \Phi_{\text{clas}})}{\Phi_0}\right). \quad (C5)$$

This is as if we had a particle with mass inversely proportional to $E_C$ in the potential $V(\hat{\phi}) = \frac{1}{2}E_L\hat{\Phi}_a^2 - E_J\cos(\frac{2\pi(\hat{\phi}_a + \Phi_{\text{clas}})}{\Phi_0})$. Bear in mind that this potential depends on the $\Phi_{\text{clas}}$ parameter and that by tuning it, we can achieve different potentials which will lead to significantly different systems. Explicitly, if we substitute of $\hat{\Phi}_a = 4k\hat{x}$, $E_C = 2\frac{k^2}{m}$, $E_J = \omega_q$, $E_L = \frac{m\omega^2}{16k^2}$, $g = (8E_L E_C^3)^{1/4}$, and $\Phi_{\text{class}} = \pi$, we arrive at an exact mapping between the atomic physics model and the superconducting circuit model. Comparing the energy scales given in [18] to the parameters used in our setup yields a relative coupling strength of $g/\omega \approx 1.91$ and a ratio between the qubit splitting and bosonic mode of $\omega_q/\omega \approx 2.42$.

## APPENDIX D: PERTURBATIVE DEEP STRONG-COUPLING REGIME: ANALYTICAL TREATMENT

In this Appendix, we present an analytical approach to derive the dynamics of the pQRM using perturbation theory. To begin, we evaluate the expectation value of the mean position $\langle x \rangle$ (see, also, in Fig. 6), employing a perturbative approach applied to the system Hamiltonian described by Eq. (1). This perturbative analysis offers a different perspective on the system Hamiltonian, complementing the approach outlined in the main text via Bloch band mapping. In earlier works regarding the spectral classification of the quantum Rabi model, it has been shown that when increasing the relative coupling strength $g/\omega$, with $\omega$ being the bosonic mode frequency to the dominating energy in the system, one moves from the "usual" deep strong-coupling regime (DSC, $g/\omega \simeq 1$) to the so-called

perturbative deep strong-coupling regime (pDSC, $g/\omega \gg 1$) [28]. It is in this limit where, in contrast to the earlier discussed regimes where the coupling strength was assumed to be a perturbation of the system, now it is the dominating energy, while the normalized qubit frequency $\omega_q/\omega$ is now regarded as the perturbation. Hence, by using perturbation theory, predictions of observables of the pQRM in a real-space description based on using the variables $x$ and $p$ can be given. To compare the effectiveness of this perturbative method with a straightforward numerical approach, we will also present the overlap and fidelity of the respective systems in the following. It is noteworthy to mention that a similar perturbative approach can be used to derive the dynamics in the QRM far in the deep strong-coupling regime using the parity symmetry of the system [10].

The Hamiltonian of the model is [see Eq. (1)]

$$H = \frac{p^2}{2m} + \frac{m\omega^2}{2}x^2 + \frac{V}{2}\cos(4kx).$$

In this note, we use the following units: $m = \hbar = \omega = 1$; then the Hamiltonian takes the form

$$H = \frac{p^2}{2} + \frac{1}{2}x^2 + \frac{V}{2}\cos(4kx). \quad (D1)$$

By standard definition,

$$x = \frac{1}{\sqrt{2}}(a^\dagger + a), \quad p = i\frac{1}{\sqrt{2}}(a^\dagger - a).$$

The Hamiltonian (D1) can be written as

$$H = a^\dagger a + \frac{1}{2} + \frac{V}{2}\cos[2g(a^\dagger + a)], \quad (D2)$$

where

$$g = 2k\sqrt{\frac{\hbar\omega}{2m}} = \sqrt{2}k.$$

For purposes of a perturbative calculation, it is convenient to choose the unperturbed wave functions as Fock states. We seek a solution of the Schrödinger equation,

$$i\frac{\partial}{\partial t}|\Psi\rangle = \left\{a^\dagger a + \frac{1}{2} + \frac{V}{2}\cos[2g(a^\dagger + a)]\right\}|\Psi\rangle, \quad (D3)$$

in the form

$$|\Psi(t)\rangle = \sum_{n=0}^{\infty} a_n(t)|n\rangle.$$

Then $a_n(t)$ obey the equation

$$i\frac{\partial}{\partial t}a_n(t) = \left(n + \frac{1}{2}\right)a_n(t)$$
$$+ \frac{V}{2}\sum_{m=0}^{\infty}\langle m|\cos[2g(a^\dagger + a)]|n\rangle a_m(t). \quad (D4)$$

If the perturbation $\frac{V}{2}\cos[2g(a^\dagger + a)]$ is small, we can replace the eigenenergy of the Hamiltonian in Eq. (D2),

$$E_n \approx n + \frac{1}{2} + \frac{V}{2}\langle n|\cos[2g(a^\dagger + a)]|n\rangle,$$

and the eigenstates by the Fock state $|n\rangle$. For the validity of the perturbation theory, the matrix elements

$$\langle n|\cos[2g(a^\dagger + a)]|m\rangle$$

must satisfy the condition

$$\frac{V}{2}|\langle m|\cos(2\sqrt{2}gx)|n\rangle| \ll |n - m|, \quad (D5)$$

for any $|m\rangle$ and $|n\rangle$ Fock states.

The cosine matrix elements can be expressed in terms of generalized Laguerre polynomials [29]. We will consider only $m = n + 2l$,

$$\langle n|\cos(2\sqrt{2}gx)|n + 2l\rangle$$
$$= \sqrt{\frac{n!}{(n+2l)!}}(-1)^l(4g^2)^l\exp(-2g^2)L_n^{2l}(4g^2). \quad (D6)$$

In this experiment, the parameter $g$ is large, which means that the average number of excitations is also large, $N \approx g^2$. This fact allows us to use the following asymptotic expression for $L_n^{2l}(4g^2)$. With this approximation, we arrive at the following expression for the maximum of the cosine matrix element:

$$\max_{n,l\neq 0}|\langle n|\cos(2\sqrt{2}gx)|n + 2l\rangle| \approx \frac{1}{\sqrt{2\pi g}}.$$

Hence, in the worst case, we demand that

$$\frac{V}{2}\frac{1}{\sqrt{2\pi g}} \ll 2. \quad (D7)$$

Then the condition (D5) will be fulfilled automatically. Or, in ordinary units,

$$\frac{V}{2\omega} = \frac{\omega_q}{\omega} \ll 2\sqrt{2\pi\frac{g}{\omega}} \approx 5\sqrt{\frac{g}{\omega}}. \quad (D8)$$

For the experimental parameters of the experimental system that is discussed here (e.g., for the data of Fig. 4, $\frac{\omega_q}{\omega} \lesssim 2$, $2\sqrt{\frac{g}{\omega}} \approx 11$), this condition is approximately fulfilled.

Upon introducing the displacement operator $D(\alpha)$, the last term in the Hamiltonian (D2) can be brought to a more pleasant form,

$$\cos[2g(a^\dagger + a)]$$
$$= \frac{1}{2}\{\exp[2ig(a^\dagger + a)] + \exp[-2ig(a^\dagger + a)]\}$$
$$= \frac{1}{2}[D(2ig) + D(-2ig)]. \quad (D9)$$

By using the representation of the displacement operator in the Fock basis (see [30]), we get

$$\langle n|D(\alpha)|n\rangle = \exp\left(-\frac{|\alpha|^2}{2}\right)L_n(|\alpha|^2),$$

where $L_n$ are the Laguerre polynomials. The eigenvalues and the solution of our problem can be written as

$$E_n \approx n + \frac{V}{2}\exp(-2g^2)L_n(4g^2),$$

$$|\Psi(t)\rangle \approx \exp[-it(A + D)]\sum_{n=0}^{\infty}a_n(0)|n\rangle, \quad (D10)$$

where $A$ and $D$ are diagonal matrices in the Fock space,

$$A_{nm} + D_{nm} = \left[n + \frac{V}{2}\exp(-2g^2)L_n(4g^2)\right]\delta_{nm}.$$

We apply the solution (D10) when the state is initially prepared as

$$|\Psi(0)\rangle \rightarrow \mathcal{N}_1[|2k\rangle + |-2k\rangle] \rightarrow \mathcal{N}_2[|ig\rangle + |-ig\rangle],$$

where $\mathcal{N}_1$ and $\mathcal{N}_2$ are normalization parameters and $|g\rangle$ is the coherent state with the displacement $g$.

After normalization, it takes the following form:

$$|\Psi(0)\rangle = \frac{1}{\sqrt{2}\sqrt{1+\exp(-2g^2)}}\exp\left(-\frac{g^2}{2}\right)\sum_{n=0}^{\infty}\frac{(ig)^n+(-ig)^n}{\sqrt{n!}}|n\rangle. \tag{D11}$$

Then the state at time $t$ is

$$|\Psi(t)\rangle = \frac{1}{\sqrt{2}\sqrt{1+\exp(-2g^2)}}\exp\left(-\frac{g^2}{2}\right)\sum_{n=0}^{\infty}\left(\frac{(ig)^n+(-ig)^n}{\sqrt{n!}}\right)\exp\left\{-it\left[n+\frac{V}{2}\exp(-2g^2)L_n(4g^2)\right]\right\}|n\rangle. \tag{D12}$$

The overlap with the initial state is equal to

$$\langle\Psi(0)|\Psi(t)\rangle = \frac{\exp(-g^2)}{2[1+\exp(-2g^2)]}\left(\sum_{n=0}^{\infty}\frac{[(ig)^n+(-ig)^n]^2}{n!}\exp\left\{-it\left[n+\frac{V}{2}\exp(-2g^2)L_n(4g^2)\right]\right\}\right)$$

$$= \frac{\exp(-g^2)}{[1+\exp(-2g^2)]}\left(\sum_{n=0}^{\infty}\frac{g^{2n}[1+(-1)^n]}{n!}\exp\left\{-it\left[n+\frac{V}{2}\exp(-2g^2)L_n(4g^2)\right]\right\}\right)$$

$$= \frac{1}{\cosh(g^2)}\left(\sum_{n=0}^{\infty}\frac{g^{4n}}{(2n)!}\exp\left\{-it\left[2n+\frac{V}{2}\exp(-2g^2)L_{2n}(4g^2)\right]\right\}\right). \tag{D13}$$

### 1. Dynamics of the mean position $\langle x \rangle$

In Fig. 8, we have calculated the mean position coordinate $\langle x \rangle$ and can directly compare this observable to the numerical solution which was used in the main text and in the Appendix to calculate the theoretical predictions for the experimental data in Fig. 6. We find good agreement of the perturbative method with the behavior of the mean position, which among other things is used to calculate the bosonic excitation number in Fig. 2.

### 2. Overlap $|\langle \Psi(0)|\Psi(t)\rangle|^2$

In Figs. 9 and 10, we compare the overlap $|\langle \Psi(0)|\Psi(t)\rangle|^2$ obtained from the numerical solution of Eq. (D3) for the initial state (D11) with the overlap according to Eq. (D13). A notable feature of this expression is that due to the anharmonic nature of the spectrum, the wave function does not recover after one oscillator period. Moreover, it quite accurately predicts the amplitude of the overlap of the wave function with the
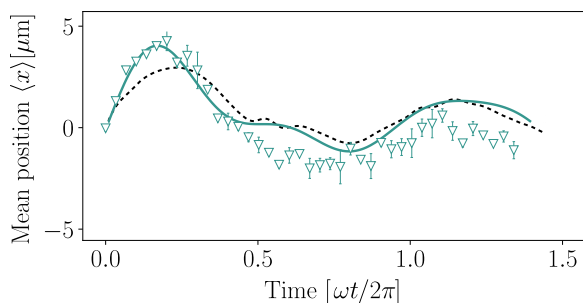
initial state. There is room to improve the accuracy of this perturbative solution by taking into account higher-order corrections. However, these correction are outside of the scope of this paper.

### 3. Fidelity $|\langle \Psi_p(t)|\Psi(t)\rangle|$

In order to further justify the validity of this alternative method, we have calculated the fidelity of the exact and perturbative solutions,

$$F(t) = \left|\langle\Psi_p(t)|\Psi(t)\rangle\right|,$$

where $|\Psi(t)\rangle$ is the exact solution of the Schrödinger equation and $|\Psi_p(t)\rangle$ is the perturbative one [see Eq. (D10)], with



FIG. 8. Temporal evolution of the measured values for the mean atomic position $\langle x \rangle$ for a qubit frequency of $\omega_q/2\pi = 1750(25)\,\text{Hz}$ (green data points), along with theory based on the periodic quantum Rabi model (dotted black lines) and the perturbative approach presented above. Experimental parameters are as in Fig. 3.
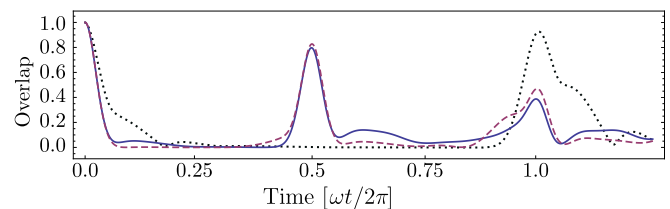


FIG. 9. Variation of the overlap $|\langle\Psi(0)|\Psi(t)\rangle|^2$ vs time (units of $\omega t/2\pi$). The initial state here is $\frac{1}{\sqrt{2}}[|2k\rangle + |-2k\rangle]$. The other parameters are $\frac{\omega_q}{\omega} = \frac{V}{2\omega} = \frac{1280}{650} \approx 1.96$, $\frac{g}{\omega} = 4.8$, the same as in Fig. 4. The blue line corresponds to the numerical calculations of Eq. (D3). The purple dashed line corresponds to the perturbative analytic expression (D13). The black dotted line is the numerical calculation of the "usual" QRM (see, also, Fig. 4), which, as mentioned before, shows temporal dynamics at half of the periodicity of the pQRM (first revival at $\omega t/2\pi = 1$).
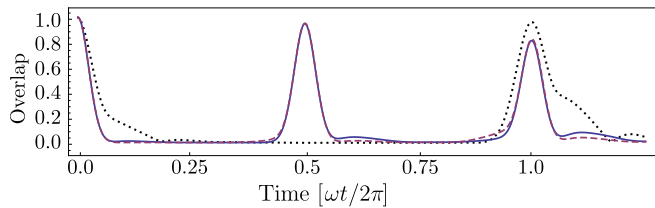
FIG. 10. Same as in Fig. 9, but for a smaller value of the qubit splitting, $\frac{\omega_q}{\omega} = 1.2$.

the initial state

$$|\Psi(0)\rangle = \exp\left(-\frac{g^2}{2}\right)\sum_{n=0}^{\infty}\frac{(-ig)^n}{\sqrt{n!}}|n\rangle. \qquad (D14)$$
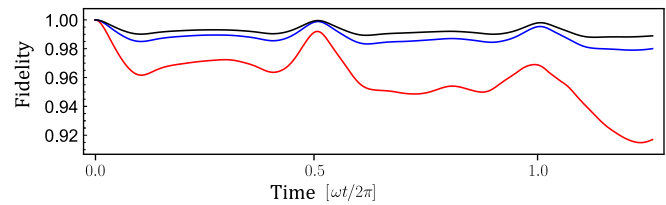


FIG. 11. Temporal evolution of the fidelity $F(t) = |\langle\Psi_p(t)|\Psi(t)\rangle|$ for different values of the qubit frequency: $\omega_q/2\pi = 650\,\text{Hz}$ (black), $800\,\text{Hz}$ (blue), and $1280\,\text{Hz}$ (red).

As can be seen in Fig. 11, there is good agreement between the exact solution and the perturbative method. Increasing the qubit frequency leads to a larger deviation in the calculated value for $F(t)$, which is expected.

[1] I. I. Rabi, On the process of space quantization, Phys. Rev. **49**, 324 (1936).

[2] D. Braak, Q.-H. Chen, M. T. Batchelor, and E. Solano, Semi-classical and quantum Rabi models: In celebration of 80 years, J. Phys. A: Math. Theor. **49**, 300301 (2016).

[3] S. Haroche and J.-M. Raimond, *Exploring the Quantum: Atoms, Cavities, and Photons* (Oxford University Press, Oxford, 2006).

[4] E. Jaynes and F. Cummings, Comparison of quantum and semi-classical radiation theories with application to the beam maser, Proc. IEEE **51**, 89 (1963).

[5] H. Häffner, C. Roos, and R. Blatt, Quantum computing with trapped ions, Phys. Rep. **469**, 155 (2008).

[6] P. Forn-Díaz, L. Lamata, E. Rico, J. Kono, and E. Solano, Ultrastrong coupling regimes of light-matter interaction, Rev. Mod. Phys. **91**, 025005 (2019).

[7] N. K. Langford, R. Sagastizabal, M. Kounalakis, C. Dickel, A. Bruno, F. Luthi, D. J. Thoen, A. Endo, and L. Dicarlo, Experimentally simulating the dynamics of quantum light and matter at deep-strong coupling, Nat. Commun. **8**, 1715 (2017).

[8] D. Marković, S. Jezouin, Q. Ficheux, S. Fedortchenko, S. Felicetti, T. Coudreau, P. Milman, Z. Leghtas, and B. Huard, Demonstration of an effective ultrastrong coupling between two oscillators, Phys. Rev. Lett. **121**, 040505 (2018).

[9] C. Ciuti, G. Bastard, and I. Carusotto, Quantum vacuum properties of the intersubband cavity polariton field, Phys. Rev. B **72**, 115303 (2005).

[10] J. Casanova, G. Romero, I. Lizuain, J. J. García-Ripoll, and E. Solano, Deep strong coupling regime of the Jaynes-Cummings model, Phys. Rev. Lett. **105**, 263603 (2010).

[11] B. Peropadre, P. Forn-Díaz, E. Solano, and J. J. García-Ripoll, Switchable ultrastrong coupling in circuit qed, Phys. Rev. Lett. **105**, 023601 (2010).

[12] A. Dareau, Y. Meng, P. Schneeweiss, and A. Rauschenbeutel, Observation of ultrastrong spin-motion coupling for cold atoms in optical microtraps, Phys. Rev. Lett. **121**, 253603 (2018).

[13] D. Lv, S. An, Z. Liu, J.-N. Zhang, J. S. Pedernales, L. Lamata, E. Solano, and K. Kim, Quantum simulation of the quantum Rabi model in a trapped ion, Phys. Rev. X **8**, 021027 (2018).

[14] F. Yoshihara, T. Fuse, S. Ashhab, K. Kakuyanag, S. Saito, and K. Semba1, Superconducting qubit–oscillator circuit beyond the ultrastrong-coupling regime, Nat. Phys. **13**, 44 (2017).

[15] A. Bayer, M. Pozimski, S. Schambeck, D. Schuh, R. Huber, D. Bougeard, and C. Lange, Terahertz light-matter interaction beyond unity coupling strength, Nano Lett. **17**, 6340 (2017).

[16] M.-L. Cai, Z.-D. Liu, W.-D. Zhao, Y.-K. Wu, Q.-X. Mei, Y. Jiang, L. He, X. Zhang, Z.-C. Zhou, and L.-M. Duan, Observation of a quantum phase transition in the quantum Rabi model with a single trapped ion, Nat. Commun. **12**, 1126 (2020).

[17] J. Koch, G. R. Hunanyan, T. Ockenfels, E. Rico, E. Solano, and M. Weitz, Quantum Rabi dynamics of trapped atoms far in the deep strong coupling regime, Nat. Commun. **14**, 954 (2023).

[18] I. V. Pechenezhskiy, R. A. Mencia, L. B. Nguyen, Y. H. Lin, and V. E. Manucharyan, The superconducting quasicharge qubit, Nature (London) **585**, 368 (2020).

[19] G. Ritt, C. Geckeler, T. Salger, G. Cennini, and M. Weitz, Fourier synthesis of optical potentials for atomic quantum gases, Phys. Rev. A **74**, 063622 (2006).

[20] T. Salger, C. Geckeler, S. Kling, and M. Weitz, Atomic Landau-Zener tunneling in Fourier-synthesized optical lattices, Phys. Rev. Lett. **99**, 190405 (2007).

[21] S. Felicetti, E. Rico, C. Sabin, T. Ockenfels, J. Koch, M. Leder, C. Grossert, M. Weitz, and E. Solano, Quantum Rabi model in the Brillouin zone with ultracold atoms, Phys. Rev. A **95**, 013827 (2017).

[22] F. A. Wolf, M. Kollar, and D. Braak, Exact real-time dynamics of the quantum Rabi model, Phys. Rev. A **85**, 053817 (2012).

[23] V. E. Manucharyan, J. Koch, L. I. Glazman, and M. H. Devoret, Fluxonium: Single Cooper-pair circuit free of charge offsets, Science **326**, 113 (2009).

[24] L. Lamata, A. Parra-Rodriguez, M. Sanz, and E. Solano, Digital-analog quantum simulations with superconducting circuits, Adv. Phys.: X **3**, 1457981 (2018).

[25] M.-J. Hwang, R. Puebla, and M. B. Plenio, Quantum phase transition and universal dynamics in the Rabi model, Phys. Rev. Lett. **115**, 180404 (2015).

[26] M. Heyl, Dynamical quantum phase transitions: A review, Rep. Prog. Phys. **81**, 054001 (2018).

[27] Y.-T. Yang and H.-G. Luo, Characterizing superradiant phase of the quantum Rabi model, Chin. Phys. Lett. **40**, 020502 (2023).

[28] D. Z. Rossatto, C. J. Villas-Bôas, M. Sanz, and E. Solano, Spectral classification of coupling regimes in the quantum Rabi model, Phys. Rev. A **96**, 013849 (2017).

[29] S. Gradshteyn and I. M. Ryzhik, *Table of Integrals, Series, and Products*, 7th ed. (Academic Press, San Diego, 2007), p. 806.

[30] K. E. Cahill and R. J. Glauber, Ordered expansions in boson amplitude operators, Phys. Rev. **177**, 1857 (1969).